

Free energy barrier and thermal-quantum behavior of sliding bilayer graphene

Jean Paul Nery,^{1,2,3,*} Lorenzo Monacelli,¹ and Francesco Mauri^{1,2,†}

¹*Dipartimento di Fisica, Università di Roma La Sapienza, I-00185 Roma, Italy*

²*Graphene Labs, Fondazione Istituto Italiano di Tecnologia, Via Morego, I-16163 Genova, Italy*

³*Nanomat group, QMAT research unit, and European Theoretical Spectroscopy Facility, Université de Liège, B5a allée du 6 août, 19, B-4000 Liège, Belgium*

In multilayer graphene, the stacking order of the layers plays a crucial role in the electronic properties and the manifestation of superconductivity. By applying shear stress, it is possible to induce sliding between different layers, altering the stacking order. Here, focusing on bilayer graphene, we analyze how ionic fluctuations alter the free energy barrier between different stacking equilibria. We calculate the free energy barrier through the state-of-the-art self-consistent harmonic approximation, which can be evaluated at unstable configurations. We find that above 100 K there is a large reduction of the barrier of more than 30% due to thermal vibrations, which significantly improves the agreement between previous first-principles theoretical work and experiments in a single graphite crystal. As the temperature increases, the barrier remains nearly constant up to around 500 K, with a more pronounced decrease only at higher temperatures. Our approach is general and paves the way for systematically accounting for thermal effects in free energy barriers of other macroscopic systems.

I. INTRODUCTION

There has been intense research on graphene since its discovery in 2004, and also on multilayer graphene systems. Among many other interesting properties, flat bands are present in multilayer rhombohedral (ABC-stacked) graphene (RG)¹, and superconductivity has been observed in RG in 2021². Several works recently studied, both experimentally and theoretically, under which conditions RG can form^{3–8}. In particular, some of us unveiled how the stacking of graphene layers changes under shear stress⁹, and obtained that it produces many consecutive layers of RG. In fact, all samples with long-range RG that have been observed so far have been subject to some form of shear stress^{5,10–14}.

To move graphene layers with respect to each other, they have to overcome a free energy barrier that separates different minima. When doing so, they experiment “stick-slip” motion: they move gradually with increasing shear stress, followed by sudden rearrangements and decrease of the stress¹⁵. The maximum shear-stress to “unlock” layers is correlated with the height of the barrier. Such barrier corresponds to the activation energy of a metastable state, where a graphene flake sitting on top of a large graphene layer is displaced relative to the equilibrium position.

Superlubricity is a another phenomenon where the energy landscape corresponding to the relative displacement of layers is also central. In this mechanism, which has attracted a lot attention^{16,17}, particularly in carbon-based systems like multilayer graphene and graphite, incommensurate surfaces (i.e. atomic lattices without matching periodicity) lead to extremely low friction. Yet another phenomena involving sliding surfaces

is thermolubricity, which refers to the assistance from thermal excitations to overcome barriers. This term has been coined by some works that have studied the transition from stick-slip motion into stochastic fluctuations in friction at sufficiently high temperatures¹⁸. Despite the interest in sliding surfaces, there are no studies that account for both temperature and quantum effects of free-energy barriers in macroscopic systems. A few works have studied quantum effects in free-energy barriers, including zero-point renormalization and tunneling, but of systems involving hydrogen molecules, including dissociative adsorption¹⁹ and diffusion^{20–22}.

The variation of the potential along a periodic crystal surface, combined with the attraction between layers, prevents free sliding between them. This phenomenon has been extensively studied in various systems, like graphite²³, MoS₂²⁴, silicon on gold²⁵, among others. When using a tip with the goal of sliding layers, normal forces need not be large. For pressures much lower than 1GPa, the alteration of the free-energy landscape is minimal (see SI of Ref. 9), so the relaxed barrier remains the dominant contribution that impedes sliding. In addition, some works on superlubricity have observed that friction has an extremely weak dependence with the load, attributed for example²³ to a contact area that remains nearly constant in the force range applied. Here, we focus on calculating the height of the barrier, which should be approximately proportional to the force –given by the maximum slope of the free energy profile– that is needed for a layer to move from one minima to another in commensurate systems.

A quantity closely related to the free energy barrier is the shear frequency, corresponding to the mode in which layers move rigidly in-plane and out of phase around the equilibrium position. The free energy bar-

rier separates two equivalent minima, so the barrier and shear frequency are expected to have a similar temperature dependence (a lower curvature at the minima corresponds to a lower shear frequency and a lower free energy, at least close to the minima). The value of the shear frequency in graphite is a relatively well-established quantity, with experimental values²⁶ oscillating between 42 - 45 cm⁻¹, using for example inelastic X-ray scattering²⁷, neutron-coherent inelastic scattering²⁸, Raman spectra^{29,30}, and coherent phonon spectroscopy³¹. In bilayer graphene, there are some experiments with values around 30 cm⁻¹; for example, 28 ± 3 cm⁻¹ in Refs. 31 and 32, and 32 cm⁻¹ in Ref. 29. The temperature dependence of the shear modes, however, has been barely studied. Few experiments measure the temperature dependence of the shear mode, using Raman scattering in folded 2+2 (4 layer) graphene³³, or femtosecond pump-probe spectroscopy in graphite³⁴.

Another aspect of multilayer graphene and graphite that still needs further investigation and that serves as a consistency check on the adequacy of our approach is thermal expansion (TE). Ref. 35 measured it in bilayer and trilayer graphene for the first time. Ref. 36 uses the quasi-harmonic approximation (QHA), which underestimates the out-of-plane TE at low temperatures³⁷ and has a very rapid increase at high temperatures; in-plane, it also underestimates the TE at low temperatures³⁷ and overestimates it at high temperatures³⁸. Much better out-of-plane results were obtained by using path integral molecular dynamics (PIMD)³⁹, but while the TE flattens at 500 K in graphite, experimental values continue increasing^{38,40}. However, in-plane PIMD results of Ref. 39 vastly overestimate the TE.

Motivated by the aforementioned phenomena, especially by the possibility of facilitating sliding through temperature, we focus on thermal effects on the free-energy barrier. This is a very challenging problem due to the difficulty of determining the free energy in a non-equilibrium position. Here we tackle it using the state-of-the-art stochastic self-consistent harmonic approximation (SSCHA)^{41,42}. First, in Sec. II, we briefly introduce SSCHA and the QHA, and explain how the barrier is determined. Then, in Sec. III, we present our main results and compare to the height of the barrier with fixed atoms. Subsequently, using also the QHA, we calculate the temperature dependence of the shear frequency and compare to the limited experimental data available. Finally, we determine the in-plane and out-of-plane TE coefficient in bilayer graphene and graphite, and compare our results to previous theoretical and experimental work. In Sec. IV, we summarize the conclusions of our work.

II. THEORETICAL AND COMPUTATIONAL FRAMEWORK

Here, we briefly describe the QHA, SSCHA, and a new SSCHA interpolation method used to determine the barrier. A more detailed description of SSCHA can be found in Refs. 41 or 42.

A. Quasi-harmonic approximation (QHA)

In the QHA, at each value of the lattice parameters $\{a_i\}$, the free energy $F(T, \{a_i\}) = U(\{a_i\}) - TS(T, \{a_i\})$, where U is the internal energy, S the entropy and T the temperature, is given by the standard harmonic expression. That is,

$$F(T, \{a_i\}) = U_{\text{lat}}(\{a_i\}) + \frac{1}{N_q} \sum_{\mathbf{q}\nu} \frac{1}{2} \hbar \omega_{\mathbf{q}\nu}(\{a_i\}) + \frac{1}{N_q} \sum_{\mathbf{q}\nu} kT \ln \left(1 - e^{-\hbar \omega_{\mathbf{q}\nu}(\{a_i\})/kT} \right). \quad (1)$$

where $U_{\text{lat}}\{a_i\}$ is the internal energy of the lattice for a given value of the lattice parameters, N_q the number of phonon wavevectors \mathbf{q} , ν the mode, and $\omega_{\mathbf{q}\nu}$ the corresponding phonon frequency.

The value of the lattice parameters at a given temperature, $a_i(T)$, is determined by minimizing the free energy. Using an interatomic potential, the phonon frequencies at each value of the lattice parameters can be determined with little computational effort, and thus the QHA offers a quick method to determine the lattice expansion. Using first-principles calculations, phonons can be determined using density functional perturbation theory, which uses a primitive cell and is much faster than frozen phonon (finite differences) calculations in supercells. However, it does not account for the “true anharmonicity”⁴³, present at fixed values of the parameters when varying temperature. For example, it gives an increasing as opposed to decreasing temperature dependence of the G mode in graphene, due to the negative TE of the lattice parameter. Also, if the TE is negative and the lattice parameter reduces below the classical lattice value, as in the case of monolayer graphene at about 400 K (see the Supplementary Information (SI), Fig. S11), then an acoustic mode becomes unstable and the QHA is ill-defined. These issues are not present in SSCHA.

B. Stochastic self-consistent harmonic approximation (SSCHA)

In general, the free-energy of a ionic Hamiltonian $H = T + V$ is given by

$$F_H = \text{tr}(\rho_H H) + \frac{1}{\beta} \text{tr}(\rho_H \ln \rho_H), \quad (2)$$

where ρ_H is the density matrix. In SSCHA, the density matrix is restricted to a trial harmonic Hamiltonian $\mathcal{H} = T + \mathcal{V}$, and the free energy is given by

$$\mathcal{F}_H(\mathcal{H}) = \text{tr}(\rho_{\mathcal{H}} H) + \frac{1}{\beta} \text{tr}(\rho_{\mathcal{H}} \ln \rho_{\mathcal{H}}). \quad (3)$$

Due to a variational principle, $F_H \leq \mathcal{F}_H(\mathcal{H})$. The parameters of the harmonic Hamiltonian \mathcal{H} include the centroids of the atoms, which correspond to the lattice parameters a_i of the QHA, but it also includes the interatomic force constant matrix, which contains the information of all the phonon frequencies and accounts for the true anharmonicities. Thus, SSCHA has additional parameters, and is expected in general to give better results than QHA. Also, QHA does not satisfy a variational principle. It can be shown that

$$\mathcal{F}_H(\mathcal{H}) = F_{\mathcal{H}} + \int d\mathbf{R} [V(\mathbf{R}) - \mathcal{V}(\mathbf{R})] \rho_{\mathcal{H}}(\mathbf{R}), \quad (4)$$

where \mathbf{R} indicates a general ionic configuration and $\rho_{\mathcal{H}}(\mathbf{R}) = \langle \mathbf{R} | e^{-\beta \mathcal{H}} | \mathbf{R} \rangle / Z_{\mathcal{H}}$ is the probability density of finding the crystal in a generic configuration \mathbf{R} ($Z_{\mathcal{H}} = \text{tr}[e^{-\beta \mathcal{H}}]$ is the partition function). By stochastically sampling configurations \mathbf{R} for a given density matrix $\rho_{\mathcal{H}}$, and determining the gradient of the free energy with respect the harmonic parameters (centroids and force constant matrix elements), the free energy can be minimized self-consistently. SSCHA is thus a nonperturbative method, as it does not rely on a perturbative expansion: it explores configurations with amplitudes that depend on temperature, without being limited to small displacements.

Thanks to the variational ansatz, the SSCHA quantum free energy is rigorously defined, even in out-of-equilibrium and unstable configurations like SP. In contrast, the QHA cannot determine the barrier, since the harmonic frequencies are not well defined at SP.

The logarithm term in the harmonic term Eq. (1) can be hard to converge for low frequencies. Separating the total free energy as in Eq. (4) allows to interpolate the auxiliary harmonic term up to a very fine q -mesh, which is fundamental to avoid oversampling the energy of the long-ranged shear modes, while the anharmonic contribution can be properly converged already with small simulation cells. So rather than calculating $F_{\mathcal{H}}$ directly

with the grid corresponding to the SC used in the minimization procedure, the force constant matrix can be Fourier interpolated in the usual way (building the force constant in real space from the existing q -grid, and then Fourier transforming back to any desired value of \mathbf{q}), and $F_{\mathcal{H}}$ can be calculated using a dense mesh.

This procedure is followed both at SP and the equilibrium position, and the barrier is obtained by taking the difference of the corresponding free energies. More technical details are provided in the SI, Sec. S1.

The SSCHA frequencies are in principle auxiliary frequencies that minimize the free energy. In a purely harmonic system, such frequencies correspond to the physical frequencies. But in general, they have to be corrected with the so-called “bubble correction” (and also an additional higher order term in very anharmonic cases)⁴², which we do in Sec. III B to obtain the temperature dependence of the shear frequency. Convergence with the supercell size of both the physical and auxiliary frequencies can be seen in the SI, Fig. S6.

III. RESULTS

A. Barrier

We first focus on studying bilayer graphene, where the in-plane and (most importantly) out-of-plane interactions are given by the interatomic potential of Ref. 44 and Ref. 45, respectively. The out-of-plane interactions determine the barrier. The energy profile of a layer moving with respect to the other one along the bond direction is given by Fig. 1, which gives good results when comparing to theory and experiment (see Table I).

TABLE I. Comparison of the barrier V_{SP} and the shear frequency at fixed ionic positions (classical at $T = 0$ K) between the interatomic potential we used in this work^{44,45}, LDA, and theoretical calculations and experiments from previous works. The values are a little bit lower but close to that of adiabatic-connection fluctuation-dissipation theorem within the random phase approximation (ACFDT-RPA)⁴⁶ and experimental data²⁶.

	2 layers This work	2 layers LDA	Previous works
Small barrier V_{SP} (meV/atom)	1.24	1.58	1.53 (RPA) ⁴⁶
Shear frequency (cm^{-1}) (bulk)	37	42	42-45 ²⁶

The lower layer is fixed in position A, and there are two minima of the same energy, AB and AC, at a distance of a bond length $d = 1.42$ Å. For layers to slide

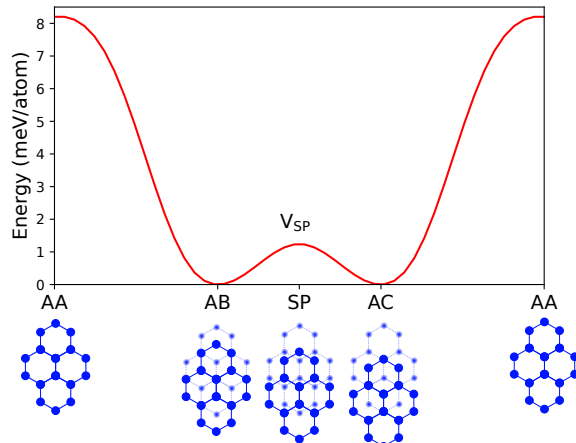


FIG. 1. Energy profile of bilayer graphene when moving one layer relative to the other along the bond direction. The lower layer is fixed in position A. Configuration AA (one layer on top of each other) is the least favorable configuration. There are two minima of the same energy, AB and AC, which correspond to the two stable configurations. To go from one minima to the other one applying shear stress, the upper layer has to overcome the barrier V_{SP} , which has a value of 1.24 meV/atom relative to the minima. The diagrams below illustrate the different configurations, with the upper layer (darker blue) moving relative to the lower one in position A (lighter blue).

with respect to each other, they have to overcome a barrier V_{SP} . SP is a saddle point in the full energy landscape, so the shear mode in the perpendicular direction (along the direction of two nearby AA maxima) is stable. In order to determine temperature effects on the barrier, we use SSCHA to determine the free energy at the equilibrium position and SP, using the interpolation method described in Sec. II B. The barrier as a function of temperature can be seen in blue in Fig. 2.

The barrier at 100 K is reduced by a substantial 35% with respect to the value at fixed nuclei. We expect intralayer modes to contribute little to the reduction of the barrier, since they should not change much when displacing the layers. On the other hand, modes involving the relative motion of the layers should be much more affected. Indeed, intralayer modes are virtually identical, so they do not contribute to a change in the barrier. Regarding the interlayer modes, the breathing mode changes little, while the shear modes do differ significantly (see Fig. S4). Thus, the shear modes are responsible for the large reduction of the barrier. This makes sense intuitively: modes that involve a relative displacement of the layers should facilitate sliding. In the fixed ion calculation, the system is exactly at SP, but in reality, the system is also exploring surrounding configurations, which have a lower energy.

Remarkably, our results show improved agreement with experiments. In a previous work⁹, using density

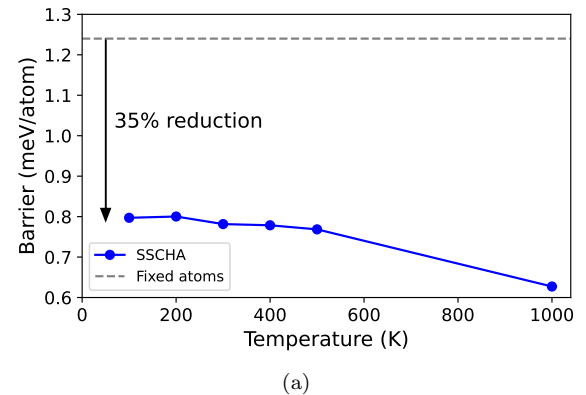


FIG. 2. Barrier as a function of temperature. It is reduced from 1.24 meV/atom, the value at fixed nuclei (V_{SP} in Fig. 1), to about 0.8 meV/atom, corresponding to a large reduction of about 35% due to phonons. The barrier does not change much up to about 500 K, but the value at 1000 K is about 20% smaller relative to the value at 100 K. The lines are a guide to the eye, as in the other figures of this work.

functional theory with an LDA functional (see Table 1), some of us obtained that the maximum shear stress in simulated stick-slip motion is 0.2 GPa, and we mentioned a good agreement with experimental values 0.14 GPa (Ref. 15) – a benchmark for defect free single crystal graphite⁴⁷ – and 0.1 GPa (Ref. 23). Assuming that the maximum shear stress decreases by 35% in line with the barrier, we now obtain 0.13 GPa, in excellent agreement with experiments^{15,23}.

Since 100 K – about 70 cm^{-1} in wavenumber units – is a relatively low temperature, quantum fluctuations may play a role. To assess their impact on the free energy barrier, we also performed calculations in the classical limit $\hbar\omega/kT \rightarrow 0$. The calculation reported in the SI indicate that quantum effects are negligible above 100 K. The reason is that shear modes responsible for the barrier reduction have very low energies, and even a modest temperature can populate such modes. This is not a general feature, as other systems present significant differences between classical and quantum free energy barriers, as in materials formed by light hydrogen atoms. Such quantum effects have been observed at 100 K (Ref. 19), 250 K (Ref. 21), and even higher temperatures²⁰.

The size of the graphene flakes considered in our work in principle correspond to nanometers up to possibly micrometer scales. In clean samples with micrometer sized flakes, different regions can have different stackings (AB and AC)^{12,48}, and a domain wall in the metastable state separates both regions. The displacement of layers in this case is more complex and is not considered in our work. We expect shear stress to be lower in this case, since the metastable state is already present. Defects

and stacking faults also lead to lower friction due to incommensurabilities, so the shear stress of 0.14 GPa corresponds to the maximum expected value⁴⁷.

In other materials, the anharmonicities associated with the unstable modes at a saddle point should also contribute negatively to the free energy. However, the overall change of the barrier will depend on differences in the entire SSCHA phonon spectra at the minima and saddle point.

Regarding the evolution of the barrier as the temperature increases, there is a weak dependence up to about 500 K, since the barrier remains close to around 0.8 meV/atom. However, when temperature increases up to 1000 K, the barrier is further reduced by 20% relative to the value at 100 K. Thus, high temperatures should facilitate sliding between layers. In particular, it could aid the production of ABC-stacked multilayer graphene from its more common AB-stacked version through shear stress, as mentioned in the Introduction. More in general, high temperatures could also help engineer specific stacking arrangements in other layered materials.

B. Shear frequency

At the equilibrium position, one of the vibrational modes at Γ is the shear mode in both directions of the plane (doubly degenerate, see Fig. 3). Its temperature dependence can be determined using both SSCHA and QHA. In the QHA, the TE is obtained by determining the lattice parameters that minimize the free energy at each temperature.

The third out of phase mode of the layers is the breathing mode, in the out-of-plane direction. A discussion of its temperature dependence can be found in the SI.

The temperature dependence of the shear frequency can be seen in Fig. 4. The quantum effects evaluated within the SSCHA harden the shear frequency energy at low temperatures compared with the classical value at 0 K (dashed line). On the other hand, the zero-point renormalization in QHA softens the shear frequency. The temperature dependence of the shear mode is similar to that of the barrier, varying by about 20% from 0 to 1000 K, and having a larger dependence at temperatures above 500 K.

Regarding the experimental data, in Ref. 33, the measurements are done in 2+2 folded graphene (4 layers). In order to compare with our 2-layer calculations, we multiply by a correction factor using a nearest-neighbor model for layers⁴⁹. In the case of bulk, such a factor is $\sqrt{2}$ (the force exerted by a layer below and above, proportional to the square of the frequency, is doubled when considering only nearest neighbor interactions), which we use to compare to the bulk measurements of

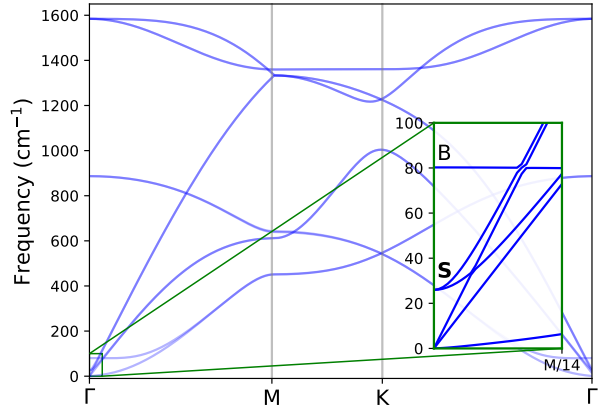


FIG. 3. Bilayer graphene phonon dispersion. The inset shows a zoom in close to Γ to better visualize the doubly degenerate shear modes **S** at Γ , and the breathing mode **B**. Due to the high speed velocity in graphene, the region of the shear mode in the BZ is small (a fraction of ΓM), and is overrepresented in small supercell calculations. The breathing mode, on the other hand, is flat, so nearby sampling points are not necessary to converge the free energy.

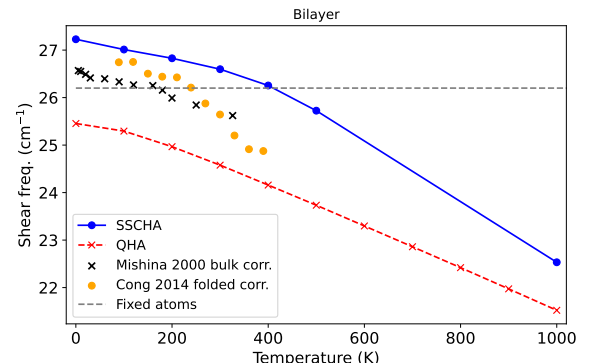


FIG. 4. Shear frequency as a function of temperature using SSCHA (blue circles) and QHA (red crosses). There is no experimental data for the temperature dependence of the shear frequency as a function of temperature for bilayer graphene. Experimental values correspond to bulk (blue crosses) and folded 2+2 graphene (orange circles), which are corrected by the factor of a nearest neighbor model⁴⁹ to compare to the bilayer case (and rigidly shifted by -5 cm^{-1} to facilitate the visual comparison). The agreement with the temperature dependence of the bulk values is good.

Ref. 34. The temperature dependence of both SSCHA and QHA curves is similar to the experimental adjusted bulk values. Folded graphene values have a steeper dependence but are likely unsuitable for comparison, because layers fold with different rotational angles, while layers are aligned in standard graphite. The shear frequency has also been measured in other materials like bilayer NbSe₂ in Ref. 49, or bulk *h*-BN in Ref. 50, which show a similar temperature dependence (adjusting the

bulk value by a $\sqrt{2}$ factor) of roughly $-0.5 \text{ cm}^{-1}/100 \text{ K}$.

C. Thermal expansion

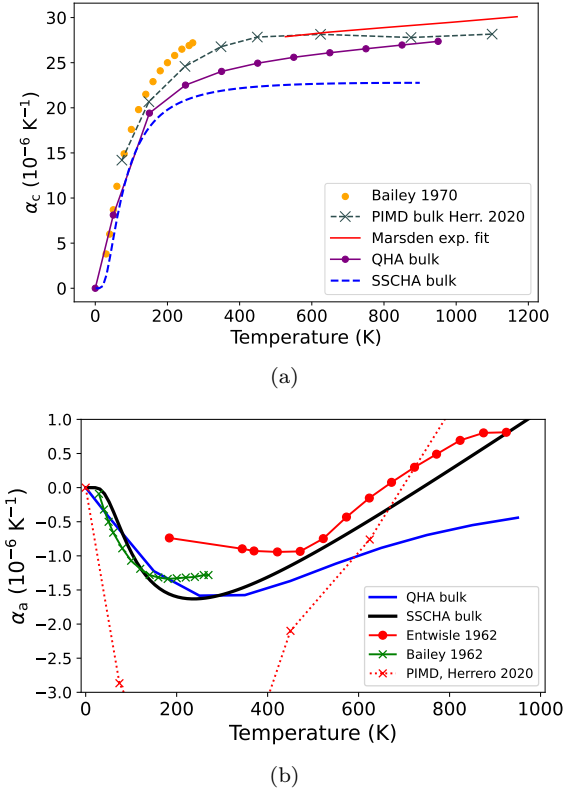


FIG. 5. (a) Graphite out-of-plane coefficient of TE as a function of temperature using SSCHA and QHA. PIMD calculations³⁹ and experimental data³⁷ are also included. PIMD overall agrees well, while QHA and SSCHA (with the potential of Ref. 45) underestimate the TE. (b) Graphite in-plane coefficient of TE using SSCHA and QHA. QHA again underestimates the dependence at low temperatures, and also at high temperatures. On the other hand, PIMD gives a dependence that is surprisingly very far from experimental values. SSCHA gives excellent results both at low and high temperatures, considering also the disagreement within experimental data.

To further check the adequacy of our method (the use of SSCHA with the in-plane⁴⁴ and out-of-plane⁴⁵ interatomic potentials), we look at the TE in the previous calculations and also in bulk graphite, and compare to experiments. The TE coefficients are given by $\alpha_a(T) = \frac{1}{a} \frac{da}{dT}$ and $\alpha_c(T) = \frac{1}{c} \frac{dc}{dT}$, with a and c the in-plane and out-of-plane lattice parameters, respectively.

In Fig. 5, we show the TE coefficient calculated with SSCHA and QHA in bulk, compared with experimental data^{37,40} and PIMD calculations³⁹. SSCHA results underestimate the TE. PIMD results are overall very

good, although they also give values somewhat lower than experiments^{37,40}.

In-plane SSCHA calculations give excellent results. QHA works well at low temperatures but departs from experiments at higher temperatures. We conducted a careful convergence of these results, reported in the SI, Sec. S3. PIMD calculations of Ref. 39, although they work very well out-of-plane, greatly overestimate in-plane TE, presumably due to the inadequacy of their interatomic potential. It would be interesting in future work to compare SSCHA and PIMD using the same potentials.

IV. CONCLUSIONS

To conclude, we demonstrated that ionic vibrations are fundamental to determining properties of layered materials that depend on free energy barriers. Using the self-consistent harmonic approximation, which can calculate the free energy at unstable configurations, and a novel interpolation method, we unveiled the suppression of the barrier separating stable configurations in bilayer graphene. Phonon vibrations reduce the free energy barrier by a significant 35%, and gets further suppressed at high temperatures, so barriers at fixed ions cannot be trusted. Now, correcting the shear stress of 0.2 GPa reported in our previous work, we arrive at a value of 0.13 GPa, in excellent agreement with experiments. The shear modes, which occupy a small region of phase space, have to be adequately sampled to correctly determine the free energy barrier as well as the thermal expansion. Although our approach underestimates the out-of-plane thermal expansion compared with experimental values, in-plane agreement with experiments is excellent. We also obtained that the temperature dependence of the barrier is similar to that of the shear frequency, which agrees well with existing measurements.

ACKNOWLEDGMENTS

This work has received funding from the European Union’s Horizon 2020 research and innovation programme under Grant Agreement No. 881603, and from the MORE-TEM ERC-SYN project, Grant Agreement No. 951215. J.P.N. is currently supported by the European Union under a Marie Skłodowska-Curie Individual Fellowship, Project GreenNP No. 101151380.

SUPPLEMENTARY INFORMATION

S1. Barrier

To determine the barrier, the free energy has to be determined at the equilibrium position and SP. At the equilibrium position, there are two shear modes, indicated with **S** in Fig. 3(b). The mode perpendicular to the bond direction shown in Fig. 1 is stable in SP, while the shear mode along the reaction coordinate (using the language of chemical reactions) is unstable. As opposed to the breathing mode, that is flat around Γ , the shear modes are only present in a small region of the BZ ($1/N^2$, with N larger than 20), as a result of the large speed of sound in graphene. So in small supercells, the shear modes will be over-represented. This is more problematic at SP, where the SSCHA frequency corresponding to the unstable mode takes very small values (see Fig. S1), which makes the convergence of the free energy hard, mostly due to the logarithm term in $F_{\mathcal{H}}$ in Eq. (4). Just determining the barrier with this equation and a $N \times N \times 1$ supercell, results in Fig. S2, which is not well converged. All SSCHA calculations used 24000 configurations, both for the barrier and the TE.

In order to get better convergence with N , we use the interpolation method mentioned in Sec. II B, and obtain a much more stable barrier as a function of $1/N$ (see Fig. S3). The 40×40 interpolation grid used for $F_{\mathcal{H}}$ corresponds to a supercell of 6400 atoms. For 100, 200 and 300 K, the barrier seems well converged. For a 1000 K, the trend seems to indicate convergence within 0.02 meV/atom, so for the intermediate temperatures 400 and 500 K, the barrier is likely also converged within a similar error, resulting in Fig. 2 of the main text.

To better understand the reduction in the barrier, we show in Fig. S4 the SSCHA frequencies (around the shear modes) at equilibrium and SP at $T = 100$ K. The SSCHA frequencies at equilibrium are similar to the standard harmonic values, as shown in the main text. The SSCHA shear frequencies at SP instead change significantly. The shear mode that looks like an acoustic mode takes a value close to 2 cm^{-1} at Γ (see also Fig. S1). The rest of the SSCHA phonon dispersion presents small differences between equilibrium and SP frequencies.

In addition, we performed calculations in the classical limit ($\hbar\omega/kT \rightarrow 0$) by increasing the carbon atomic masses by a factor of 600. This reduces the Debye temperature below 100 K, ensuring that all modes are thermally populated and recovering the classical Boltzmann distribution for the distorted configurations. As we can see in Fig. S5, the standard quantum SSCHA calculation and its classical limit coincide, showing quantum effects are negligible above 100 K.

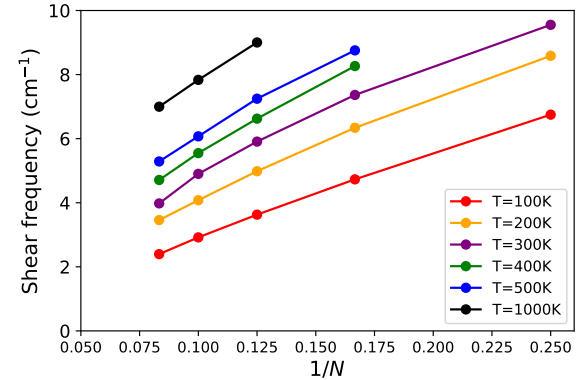


FIG. S1. Unstable shear frequency at SP as a function of $1/N$, for different temperatures. The fact that it does not stabilize shows that the shear mode is present in a small region of the BZ.

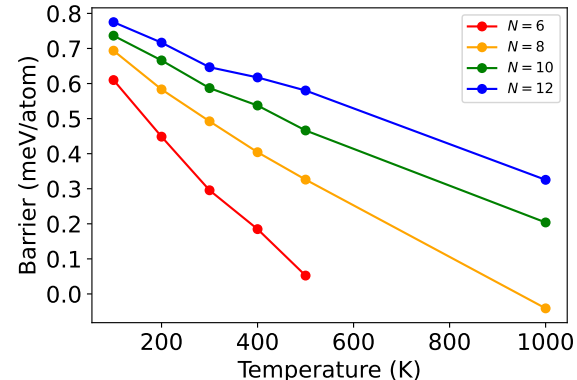


FIG. S2. Barrier as a function of temperature, for different supercells, just using the $N \times N \times 1$ grid to determine the harmonic part of the free energy Eq. (4). The barrier changes significantly with N , which means the shear mode is overrepresented. On the other hand, interpolating the harmonic part of the free energy, convergence is much better. See Fig. S3.

S2. Shear and breathing frequency

The SSCHA auxiliary and physical frequencies as a function of temperature can be observed in Fig. S6. The frequencies are not fully converged, and the converged value might be similar to the QHA. The bulk temperature dependence (corrected with the factor of the nearest neighbor model) agrees very well with QHA.

The other mode at Γ that involves the layers moving out of phase is the breathing mode (out-of-plane instead of in-plane). Its temperature dependence can be seen in Fig. S7. It decreases more at low temperatures compared to the shear mode and barrier. There are no measurements of the breathing mode as a function of temperature, so our calculations serve as a pre-

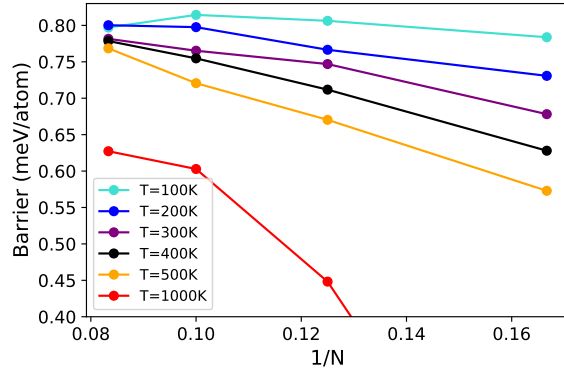


FIG. S3. Barrier as a function of $1/N$, for different temperatures, interpolating the first term of Eq. 4. The barrier seems well converged at low temperatures and harder to converge at higher temperatures. Values are likely converged within less than 0.05 meV/atom.

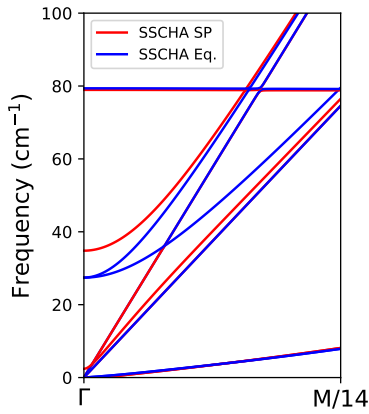


FIG. S4. SSCHA frequencies around the shear modes, at the equilibrium position (blue) and SP (red).

dition. The SSCHA curve is very well converged, so we expect it to have a temperature dependence that is closer to the experiment relative to the QHA curve. The auxiliary frequency for $N = 8$ and 10 is almost the same (Fig. S8), so the physical values are also converged (within 0.5 cm^{-1} at 1000 K , and less for lower temperatures).

S3. Thermal expansion (TE)

For the SSCHA out-of-plane TE calculations, we also used the interpolation scheme with a 40×40 grid. The interlayer distance and in-plane lattice parameter obtained in bulk with SSCHA can be seen in Fig. S9. The fits are used to reduce numerical error, and correspond Eq. (6) of Ref. 51,

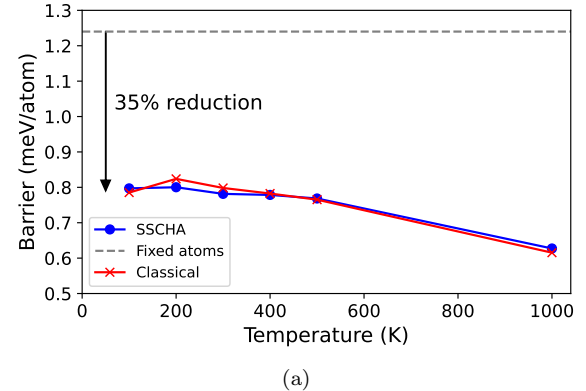


FIG. S5. Comparison between the standard quantum SSCHA results and its classical limit.

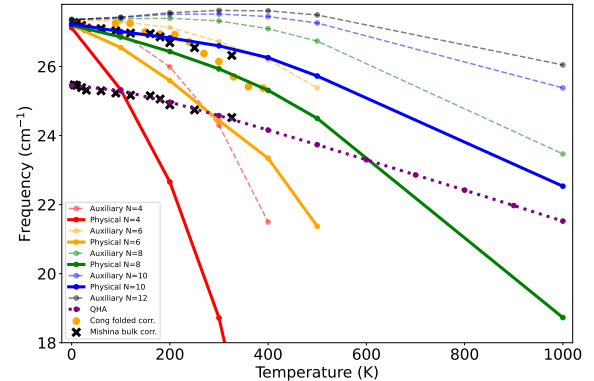


FIG. S6. Shear frequency as a function of temperature, both for the physical frequency (full lines) and the auxiliary one (dashed). The experimental value is shifted and included twice, to facilitate the comparison of the temperature dependence with the QHA and SSCHA curves. The agreement of the experimental bulk value (adjusted with the nearest neighbor model to the bilayer case) with QHA is excellent, and with SSCHA is very good as well.

$$b(T) = b_0 \exp \left(\frac{X\theta}{e^{X/T} - 1} \right), \quad (S1)$$

which depends on parameters b_0 , X and θ (b can be a or c_d). The derivative of the fits give the coefficients of TE. In the QHA case, the TE can be calculated quickly and accurately for many temperatures, so we just use finite differences.

In Fig. S10 we compare SSCHA and QHA for bilayer graphene and bulk. The TE for both SSCHA and QHA bulk is lower relative to bilayer. In-plane, Fig. S11, we can also see a clear reduction of the TE coefficient from monolayer to bulk. In what follows, we describe in detail convergence studies we did for SSCHA, and also for QHA calculations.

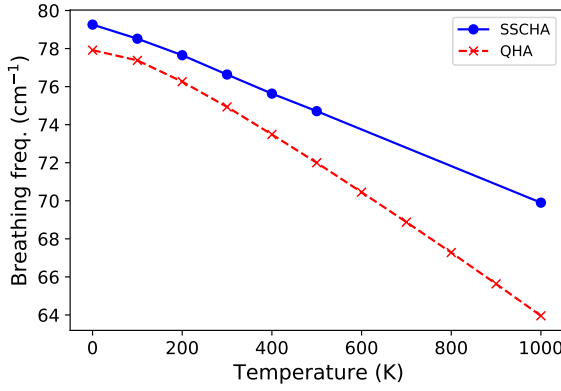


FIG. S7. Breathing frequency as a function of temperature using SSCHA (black circles) and QHA (red crosses). The SSCHA calculations are well converged and serve as a prediction, since there is no experimental data in the literature.

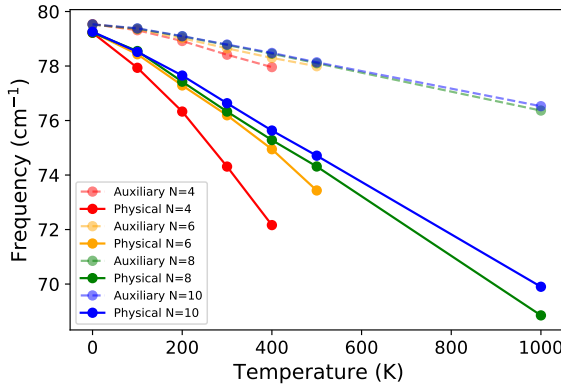


FIG. S8. Convergence of the auxiliary (dashed) and physical (full) breathing frequency. The physical frequency is well-converged at $N = 10$.

a. Bilayer

QHA. We first considered the out-of-plane TE by fixing a , and then we considered the full minimization of the free energy by varying both a and c_d . In Fig. S12 we can see $c_d(T)$ both for fixed a , and for the full minimization. The full minimization has a slightly larger dependence with temperature, but fixing a is a good approximation. Fig. S13 is analogous for $a(T)$, with a fixed value $c_d = 3.5$ Å. The curves are very similar, except for a small difference at high temperatures (of about 0.0005 Å at 1000 K).

We also studied convergence with the size of the grid (Fig. S14). At $N = 12$, $c_d(T)$ is well converged (within 0.005 Å at 1000 K), although $N \sim 20$ to achieve full convergence. The shear mode increases TE because when layers are displaced relative to each other, the inter-layer distance is larger (see Fig. S15). The monotonous

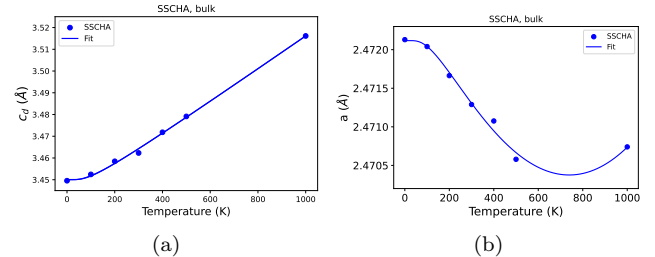


FIG. S9. Out-of plane (a) and in-plane (b) SSCHA thermal expansion (blue dots). The fit corresponds to Eq. (S1).

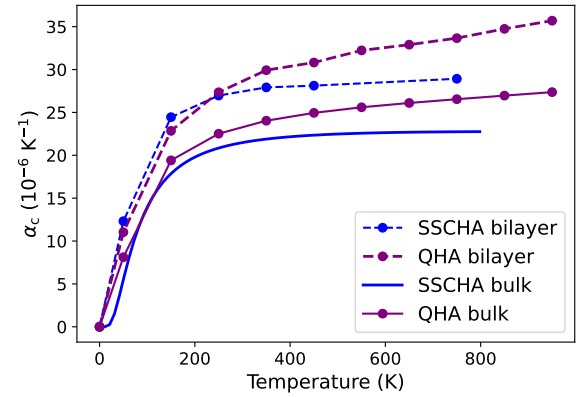


FIG. S10. SSCHA and QHA out-of-plane coefficient of TE for graphite and bilayer graphene.

behavior indicates that the shear modes are overrepresented for coarser grids, and become better sampled with denser grids (having wavevectors \mathbf{q} closer to Γ).

In-plane, a larger N of about 50 is needed to fully achieve convergence (Fig. S16). Again, monotonous convergence suggests inadequate sampling close to Γ . Since the convergence in bulk is much faster (see below Fig. S24), we attribute the slow convergence to the flexural mode, which becomes linear (an acoustic mode) and easier to sample in bulk.

SSCHA. Out-of-plane convergence is similar to the QHA case. So $N = 12$ should give a good curve for $c_d(T)$. We also see in SSCHA a similar variation of c_d when changing a (compare Figs. S12 and S19).

On the other hand, $a(T)$ has less variation with temperature relative to QHA and is already converged at about $N = 8$ (Fig. S18).

b. Bulk

QHA. In bulk, there is virtually no difference for the out-of-plane TE when fixing a , or considering also the minimization of a (Fig. S20). In-plane (Fig. S21), there is a small difference between both fixing or varying a , similar to the bilayer case.

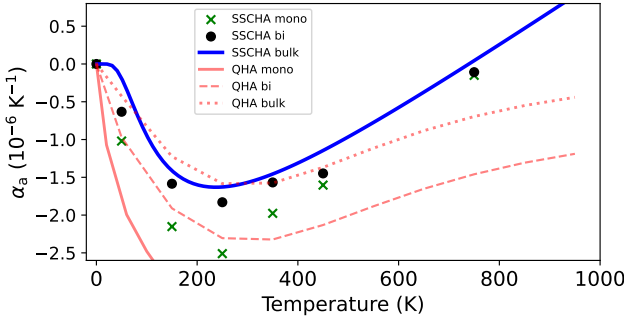


FIG. S11. In-plane coefficient of TE using SSCHA and QHA, for monolayer, bilayer and bulk.

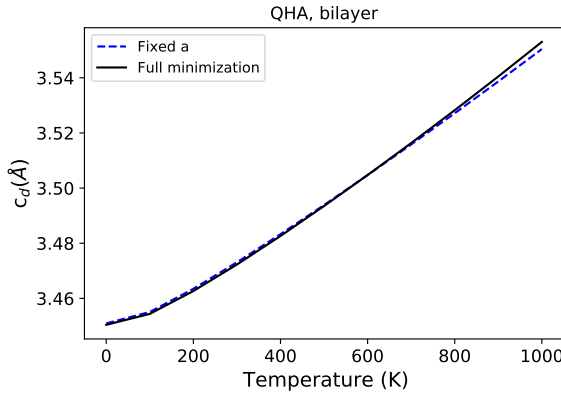


FIG. S12. Interlayer distance c_d as a function of temperature in bilayer graphene using QHA, fixing the value of a (dashed-blue) and doing the full minimization (full-black). In-plane TE has little effect on the out-of-plane TE.

Just like in the bilayer case, relative dense grids are needed to achieve out-of-plane convergence (Fig. S22), which is again likely due to the shear mode. Regarding the extension of the supercell in the out-of-plane direction, 2 unit cells (4 layers) give good results (Fig. S23). In-plane (Fig. S24), convergence is much faster than out-of-plane.

SSCHA. Here we also used the interpolation method (40×40 grid), to go beyond the $N = 8$ supercell that was possible in the direct SSCHA calculation, resulting in the blue dots of Fig. S9 (a).

In-plane, based on $N = 8$ already giving converged results in bilayer (Fig. S18), and also considering that the QHA convergence in bulk (Fig. S24) is much faster than in bilayer (Fig. S16), $N = 8$ should give converged SSCHA results in bulk, which corresponds to the blue dots in Fig. S9 (b).

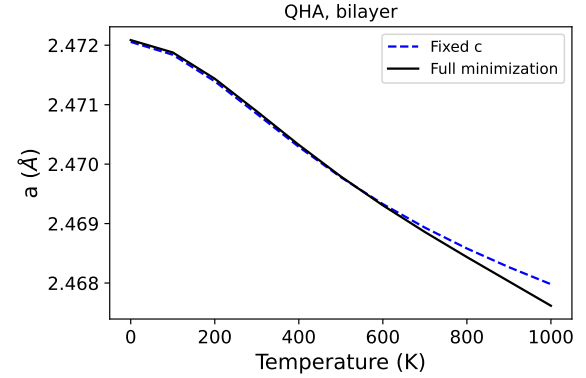


FIG. S13. Lattice parameter a as a function of temperature in bilayer graphene using QHA, fixing the value of c_d (dashed-blue) and doing the full minimization (full-black). In-plane TE has little effect on the out-of-plane TE.

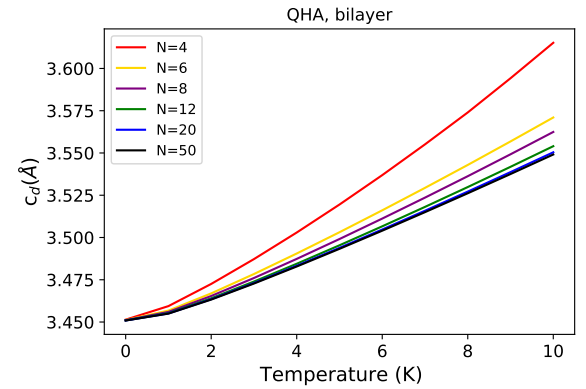


FIG. S14. Interlayer distance as a function of temperature in bilayer graphene, using QHA. At $N \sim 20$ c_d is converged, although $N = 12$ also gives a good result.

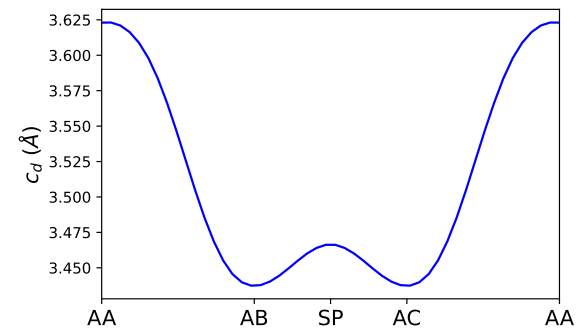


FIG. S15. Interlayer distance profile along the bond direction, when moving a graphene layer relative to another one (analogous to Fig. 1, but for distance instead of energy). The minimum distance is at the equilibrium positions.

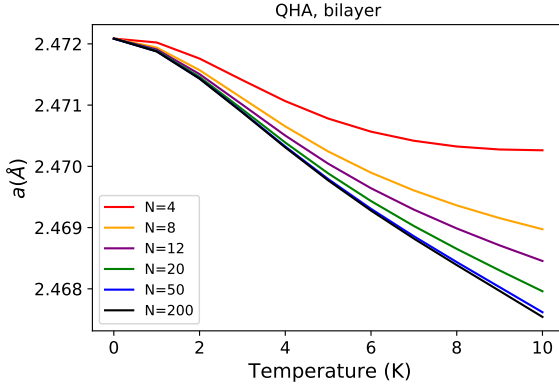


FIG. S16. In-plane lattice parameter as a function of temperature in bilayer graphene for different N using QHA. A large N is needed to achieve convergence.

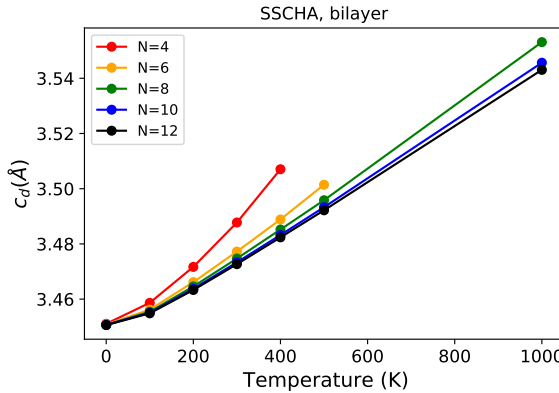


FIG. S17. Interlayer distance as a function of temperature in bilayer graphene for different N using SSCHA. Convergence is similar to the QHA case, Fig. S14, where $N = 12$ gives a good value of $c_d(T)$.

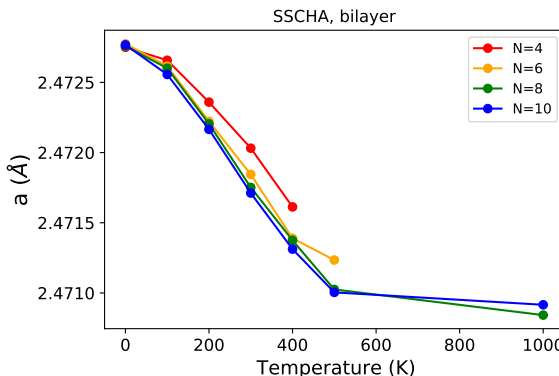


FIG. S18. In-plane lattice parameter as a function of temperature, for different N . At $N = 8$ the curve is already well converged.

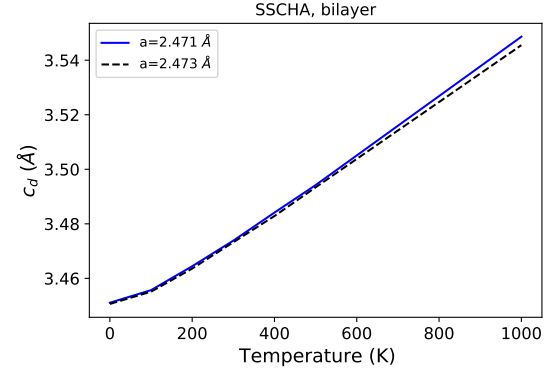


FIG. S19. Interlayer distance as a function of temperature in bilayer graphene, using SSCHA, at two different values of the in-plane lattice parameter. The curves are similar to the ones of Fig. S12. In-plane TE has little effect on the out-of-plane TE.

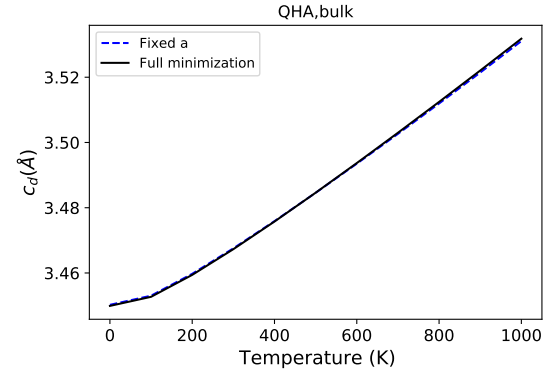


FIG. S20. Interlayer distance as a function of temperature in bulk using QHA, fixing the value of c_d (dashed-blue) and doing the full minimization (full-black). In-plane TE has barely no effect on the out-of-plane TE.

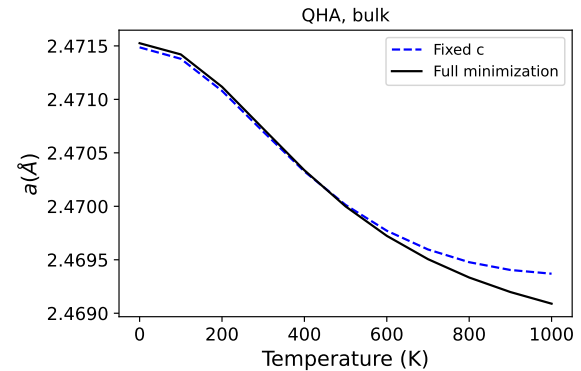


FIG. S21. In-plane lattice parameter as a function of temperature in bulk using QHA, fixing the value of c_d (dashed-blue) and doing the full minimization (full-black). The out-of-plane TE has a slightly larger but similar effect relative to bilayer on the in-plane TE.

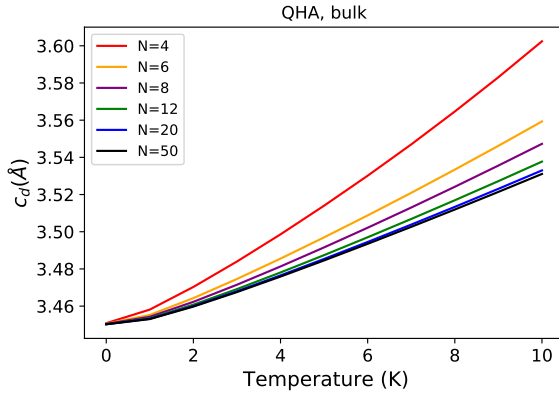


FIG. S22. Interlayer distance as a function of temperature in graphite for different N using QHA. Convergence is similar to the bilayer case.

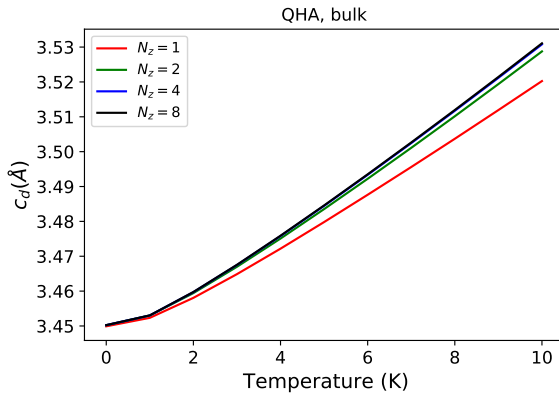


FIG. S23. Interlayer distance as a function of temperature in graphite for different N_z . $N_z = 2$ is the value used in our calculations.

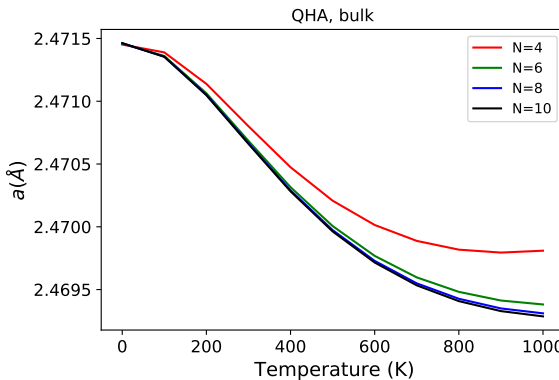


FIG. S24. In-plane lattice parameter as a function of temperature in graphite using QHA, for different N . At $N = 6$ convergence is already very good, as opposed to the bilayer case Fig. S17.

* nery.jeanpaul@gmail.com
 † francesco.mauri@uniroma1.it

¹ M. Koshino, Physical Review B **81**, 125304 (2010).

² H. Zhou, T. Xie, T. Taniguchi, K. Watanabe, and A. F. Young, Nature **598**, 434 (2021).

³ M. Yankowitz, J. I.-J. Wang, A. G. Birdwell, Y.-A. Chen, K. Watanabe, T. Taniguchi, P. Jacquod, P. San-Jose, P. Jarillo-Herrero, and B. J. LeRoy, Nature Materials **13**, 786 (2014).

⁴ F. R. Geisenhof, F. Winterer, S. Wakolbinger, T. D. Gokus, Y. C. Durmaz, D. Priesack, J. Lenz, F. Keilmann, K. Watanabe, T. Taniguchi, R. Guerrero-Avilés, M. Pelc, A. Ayuela, and R. T. Weitz, ACS Applied Nano Materials **2**, 6067 (2019).

⁵ C. Bouhafs, S. Pezzini, F. R. Geisenhof, N. Mishra, V. Mišekis, Y. Niu, C. Struzzi, R. T. Weitz, A. A. Zakharov, S. Forti, and C. Coletti, Carbon **177**, 282–290 (2021).

⁶ Z. Gao, S. Wang, J. Berry, Q. Zhang, J. Gebhardt, W. M. Parkin, J. Avila, H. Yi, C. Chen, S. Hurtado-Parra, M. Drndić, A. M. Rappe, D. J. Srolovitz, J. M. Kikkawa, Z. Luo, M. C. Asensio, F. Wang, and A. T. C. Johnson, Nature Communications **11**, 546 (2020).

⁷ H. Li, M. I. B. Utama, S. Wang, W. Zhao, S. Zhao, X. Xiao, Y. Jiang, L. Jiang, T. Taniguchi, K. Watanabe, A. Weber-Bargioni, A. Zettl, and F. Wang, Nano Letters **20**, 3106 (2020).

⁸ A. Kerelsky, C. Rubio-Verdú, L. Xian, D. M. Kennes, D. Halbertal, N. Finney, L. Song, S. Turkel, L. Wang, K. Watanabe, T. Taniguchi, J. Hone, C. Dean, D. N. Basov, A. Rubio, and A. N. Pasupathy, Proceedings of the National Academy of Sciences **118**, e2017366118 (2021).

⁹ J. P. Nery, M. Calandra, and F. Mauri, Nano Letters **20**, 5017 (2020).

¹⁰ Q. Lin, T. Li, Z. Liu, Y. Song, L. He, Z. Hu, Q. Guo, and H. Ye, Carbon **50**, 2369 (2012).

¹¹ Y. Henni, H. P. O. Collado, K. Nogajewski, M. R. Molas, G. Usaj, C. A. Balseiro, M. Orlita, M. Potemski, and C. Faugeras, Nano Letters **16**, 3710 (2016).

¹² H. Henck, J. Avila, Z. B. Aziza, D. Pierucci, J. Baima, B. Pamuk, J. Chaste, D. Utt, M. Bartos, K. Nogajewski, B. A. Piot, M. Orlita, M. Potemski, M. Calandra, M. C. Asensio, F. Mauri, C. Faugeras, and A. Ouerghi, Physical Review B **97**, 245421 (2018).

¹³ Y. Yang, Y.-C. Zou, C. R. Woods, Y. Shi, J. Yin, S. Xu, S. Ozdemir, T. Taniguchi, K. Watanabe, A. K. Geim, K. S. Novoselov, S. J. Haigh, and A. Mishchenko, Nano Letters **19**, 8526 (2019).

¹⁴ Y. Shi, S. Xu, Y. Yang, S. Slizovskiy, S. V. Morozov, S.-K. Son, S. Ozdemir, C. Mullan, J. Barrier, J. Yin, A. I. Berdyugin, B. A. Piot, T. Taniguchi, K. Watanabe, V. I. Fal'ko, K. S. Novoselov, A. K. Geim, and A. Mishchenko, Nature **584**, 210 (2020).

¹⁵ Z. Liu, S.-M. Zhang, J.-R. Yang, J. Z. Liu, Y.-L. Yang, and Q.-S. Zheng, Acta Mechanica Sinica **28**, 978–982 (2012).

¹⁶ Y. Liu, F. Grey, and Q. Zheng, Scientific Reports **4**, 4875 (2014).

¹⁷ R. C. Sinclair, J. L. Suter, and P. V. Coveney, Advanced Materials **30**, 1705791 (2018).

¹⁸ M. Z. Baykara, M. R. Vazirisereshk, and A. Martini, Applied Physics Reviews **5** (2018), 10.1063/1.5051445.

¹⁹ G. Mills and H. Jónsson, Physical Review Letters **72**, 1124 (1994).

²⁰ A. Poma, M. Monteferrante, S. Bonella, and G. Ciccotti, Physical Chemistry Chemical Physics **14**, 15458 (2012).

²¹ E. M. McIntosh, K. T. Wikfeldt, J. Ellis, A. Michaelides, and W. Allison, The Journal of Physical Chemistry Letters **4**, 1565 (2013).

²² J. R. Cendagorta, A. Powers, T. J. H. Hele, O. Marsalek, Z. Baćić, and M. E. Tuckerman, Physical Chemistry Chemical Physics **18**, 32169 (2016).

²³ M. Dienwiebel, G. S. Verhoeven, N. Pradeep, J. W. M. Frenken, J. A. Heimberg, and H. W. Zandbergen, Physical Review Letters **92**, 126101 (2004).

²⁴ M. Li, J. Shi, L. Liu, P. Yu, N. Xi, and Y. Wang, Science and Technology of Advanced Materials **17**, 189–199 (2016).

²⁵ X.-Z. Liu, Z. Ye, Y. Dong, P. Egberts, R. Carpick, and A. Martini, Physical Review Letters **114** (2015), 10.1103/physrevlett.114.146102.

²⁶ I. V. Lebedeva, A. V. Lebedev, A. M. Popov, and A. A. Knizhnik, Computational Materials Science **128**, 45 (2017).

²⁷ M. Mohr, J. Maultzsch, E. Dobardžić, S. Reich, I. Milošević, M. Damnjanović, A. Bosak, M. Krisch, and C. Thomsen, Physical Review B **76**, 035439 (2007).

²⁸ R. Nicklow, N. Wakabayashi, and H. G. Smith, Physical Review B **5**, 4951 (1972).

²⁹ P. H. Tan, W. P. Han, W. J. Zhao, Z. H. Wu, K. Chang, H. Wang, Y. F. Wang, N. Bonini, N. Marzari, N. Pugno, G. Savini, A. Lombardo, and A. C. Ferrari, Nature Materials **11**, 294 (2012).

³⁰ M. Hanfland, H. Beister, and K. Syassen, Physical Review B **39**, 12598 (1989).

³¹ D. Boschetto, L. Malard, C. H. Lui, K. F. Mak, Z. Li, H. Yan, and T. F. Heinz, Nano Letters **13**, 4620 (2013).

³² M. H. S Amelinckx, P Delavignette, Chem. Phys. Carbon **1** (1965).

³³ C. Cong and T. Yu, Nature communications **5**, 1 (2014).

³⁴ T. Mishina, K. Nitta, and Y. Masumoto, Physical Review B **62**, 2908 (2000).

³⁵ G. A. McQuade, A. S. Plaut, A. Usher, and J. Martin, Applied Physics Letters **118**, 203101 (2021).

³⁶ R. Mittal, M. K. Gupta, B. Singh, S. Mishra, and S. L. Chaplot, Solid State Communications **332**, 114324 (2021).

³⁷ A. C. Bailey and B. Yates, Journal of Applied Physics **41**, 5088 (1970).

³⁸ W. Morgan, Carbon **10**, 73 (1972).

³⁹ C. P. Herrero and R. Ramírez, Physical Review B **101**, 035405 (2020).

⁴⁰ B. Marsden, A. Mummery, and P. Mummery, Proceedings of the Royal Society A: Mathematical, Physical and Engineering Sciences **474**, 20180075 (2018).

⁴¹ I. Errea, M. Calandra, and F. Mauri, Physical Review B **89**, 064302 (2014).

⁴² L. Monacelli, R. Bianco, M. Cherubini, M. Calandra, I. Errea, and F. Mauri, *Journal of Physics: Condensed Matter* **33**, 363001 (2021).

⁴³ P. B. Allen, *Modern Physics Letters B* **34**, 2050025 (2019).

⁴⁴ F. Libbi, N. Bonini, and N. Marzari, *2D Materials* **8**, 015026 (2020).

⁴⁵ M. Wen, S. Carr, S. Fang, E. Kaxiras, and E. B. Tadmor, *Physical Review B* **98**, 235404 (2018).

⁴⁶ S. Zhou, J. Han, S. Dai, J. Sun, and D. J. Srolovitz, *Physical Review B* **92**, 155438 (2015).

⁴⁷ N. Blomquist, M. Alimadadi, M. Hummelgård, C. Dahlström, M. Olsen, and H. Olin, *Scientific Reports* **9** (2019), 10.1038/s41598-019-45133-y.

⁴⁸ L. Jiang, S. Wang, Z. Shi, C. Jin, M. I. B. Utama, S. Zhao, Y.-R. Shen, H.-J. Gao, G. Zhang, and F. Wang, *Nature Nanotechnology* **13**, 204–208 (2018).

⁴⁹ R. He, J. van Baren, J.-A. Yan, X. Xi, Z. Ye, G. Ye, I.-H. Lu, S. M. Leong, and C. H. Lui, *2D Materials* **3**, 031008 (2016).

⁵⁰ R. Cuscó, J. H. Edgar, S. Liu, G. Cassabois, B. Gil, and L. Artús, *Physical Review B* **99**, 085428 (2019).

⁵¹ J. E. Zorzi and C. A. Perottoni, *Computational Materials Science* **199**, 110719 (2021).